Biogeosciences

Carbon Flux Explorer optical assessment of C, N and P fluxes

Hannah L. Bourne[1], James K. B. Bishop[1,2], Todd J. Wood[2], Timothy J. Loew[2], and Yizhuang Liu[1]

[1]Department of Earth and Planetary Sciences, University of California, Berkeley, 94720, USA
[2]Lawrence Berkeley National Laboratory, Berkeley, 94720, USA

Correspondence: Hannah L. Bourne (hbourne@berkeley.edu)

Abstract. The magnitude and controls of particulate carbon exported from surface waters and its remineralization at depth are poorly constrained. The Carbon Flux Explorer (CFE), a Lagrangian float-deployed imaging sediment trap, has been designed to optically measure the hourly variations of particle flux to kilometer depths for months to seasons while relaying data in near-real time to shore via satellite without attending ships. The main optical proxy for particle load recorded by the CFE, volume attenuance (VA; units of mATN cm^2), while rigorously defined and highly precise, has not been robustly calibrated in terms of particulate organic carbon (POC), nitrogen (PN) and phosphorus (PP). In this study, a novel 3-D-printed particle sampler using cutting edge additive manufacturing was developed and integrated with the CFE. Two such modified floats (CFE-Cals) were deployed a total of 15 times for 18–24 h periods to gain calibration imagery and samples at depths near 150 m in four contrasting productivity environments during the June 2017 California Current Ecosystem Long-Term Ecological Research (LTER) process study. Regression slopes for VA : POC and VA : PN (units mATN cm^2 : mmol; R^2, n, p value in parentheses) were 1.01×10^4 (0.86, 12, < 0.001) and 1.01×10^5 (0.86, 15, < 0.001), respectively, and were not sensitive to particle size classes or the contrasting environments encountered. PP was not well correlated with VA, reflecting the high lability of P relative to C and N. The volume attenuance flux (VAF) to POC flux calibration is compared to previous estimates.

1 Introduction

Marine phytoplankton account for about half (or 50 Pg C yr^{-1}) of global primary productivity and live for 1 week on average before being consumed by zooplankton (Falkowski et al., 1998). Approximately 10 Pg C yr^{-1} is exported from the surface layer as sinking aggregates containing both particulate organic and inorganic carbon (POC and PIC). The carbon that reaches the deep ocean remains isolated from the atmosphere for centuries. This process, the "biological carbon pump" (BCP), is a fundamental player in the global carbon cycle, yet the stability of the BCP and its future in the face of climate-forced circulation changes and ocean acidification are currently unknown. Recent studies have noted discrepancies in reconciling mesopelagic and bathypelagic activity with current euphotic zone flux estimates (Banse, 2013; Burd et al., 2010; Ebersbach et al., 2011; Passow, 2012; Stanley et al., 2012). Furthermore, estimates of carbon flux out of the euphotic zone range widely from 6 to 12 Pg C yr^{-1} (Dunne et al., 2005; Siegel et al., 2014; Yao and Schlitzer, 2013). More traditional methods of measuring particle flux in the ocean rely on sediment traps or geochemical sampling that require ship time (Buessler et al., 2007). As ship time is expensive both in terms of funding and labor, flux measurements conducted this way are temporally and spatially limited. In recent years, there have been a number of developments towards autonomous instruments capable of measuring particle flux using optical methods (Bishop et al., 2004, 2016; Briggs et al., 2011; Estapa et al., 2013, 2017).

The attenuation of light by particles has long been used by oceanographers as a measurement of particle concentration in the ocean water column, beginning with the development of underwater transmissometers in the early 1970s

(Zaneveld, 1973). The transmissometer beam attenuation coefficient (at 660 or 650 nm) has been shown to strongly correlate with measurements of POC concentration in the water column (Bishop et al., 1999; Bishop and Wood, 2008; Boss et al., 2015; Gardner et al., 2000). Transmissometers were first deployed vertically mounted on Lagrangian profiling floats (called the Carbon Explorers, CEs) in 2001 in the North Pacific (Bishop et al., 2002). These deployments revealed a systematic loss of transmission as the CEs drifted at depth between profiles. A trend of increasing transmission was seen in the deepest 200–300 m as the CEs rose from 1000 m to the surface, implying that particles had accumulated on the upward-looking transmissometer window during drift and were being washed off during initial stages of profiling. CEs deployed in the Southern Ocean in 2002 were modified to measure transmittance before and after exhaust flow from the float's conductivity–temperature-depth (CTD) pump was used to clean particles off the transmissometer window during drift, and thus a carbon flux index (CFI) was derived as a systematic measure of particle flux over time (Bishop et al., 2004; Bishop and Wood, 2009). Estapa et al. (2017) advanced the quantitative use of float-deployed transmissometers to estimate particulate carbon flux and more properly derived a flux proxy based on beam attenuation change over the 1–2 days that their neutrally buoyant traps drifted at depth. The Estapa et al. (2017) method does not involve optics flushing.

The Carbon Flux Explorer (CFE), which combines an imaging optical sedimentation recorder (OSR) and profiling Sounding Ocean Lagrangian Observer (SOLO) float, periodically images particles as they accumulate on a glass sample stage. It thus builds upon the concept of optically measuring particle flux by quantifying particle attenuation at each pixel (Bishop et al., 2016). The imaging instrument also fully resolves particle classes from 20 μm to centimeter scale. As transmissometer beam attenuation coefficient was found to be highly correlated with POC concentration within the upper 1000 m of the ocean, a reasonable assertion would be that light attenuance of particles integrated across an image (volume attenuance) would also be highly correlated with POC load. Image attenuance (ATN) is the combined effect of both light scattering loss and light absorption by particles; it is calculated by taking the $-\log_{10}$ of a transmitted light image normalized by an in situ blank composite image of the particle-free sample stage (Bishop et al., 2016). Integration of ATN across the sample stage area yields volume attenuance (VA, units: mATN cm^2), a measure of particle load. Normalizing by trap opening and time deployed yields volume attenuance flux (VAF; units: mATN cm^2 cm^{-2} d^{-1}).

Successful calibration of VAF in carbon units would allow for far greater temporal and spatial resolution of carbon export than possible with ships and thus inform current models of biological carbon flux as CFEs have the capability of observing hourly variation in particle flux at depth for months to seasons (Bishop et al., 2016). An ear-

lier attempt to calibrate the CFE in 2013 used a surface-tethered OSR and sampler (shown in Mcdonnell et al., 2015, Fig. 3f). This method failed as it was discovered that simultaneously deployed surface-tethered OSRs and Lagrangian CFEs collected far different particle types, size distributions and quantities of material (Bishop et al., 2016). The surface-tethered OSR was biased low due to "baffle bounce" by as much as a factor of 20 and collected almost no material larger than 1.5 mm; in other words, the larger aggregates encounter the centimeter-sized openings of the tethered trap in a near-horizontal trajectory and thus bounce back into the flow rather than accumulating in the trap. The samples from the surface-tethered OSR were analyzed for phosphorus as a POC proxy, but this approach was not productive as will be shown below. Lacking appropriate calibration samples, Bishop et al. (2016) utilized aggregate size and POC weight estimates from Bishop et al. (1978) to derive a factor of 2.8 for scaling VAF (mATN cm^2 cm^{-2} d^{-1}) to POC flux (mmol C m^{-2} d^{-1}); they note that applying the Alldredge (1998) volume POC formula for marine snow particles collected by scuba divers in shallow waters yielded a conversion factor of 0.16, about 17 times smaller than the estimate based on Bishop et al. (1978).

Estapa et al. (2017), working in oligotrophic waters near Bermuda, compared sediment trap POC flux with transmissometer (650 nm) attenuation drift; conversion of their results (Fig. 7 in Estapa et al., 2017) in our units of VAF : POC yielded factors ranging from 0.46 to 0.74, 4 to 6 times lower than the 2.8 conversion factor. We note that a $\log_{10}$ to ln conversion error in Estapa et al. (2017) implied a greater difference. Multiple optical reasons for differences may include the following: (1) beam collimation (CFE uses a diffuse LED light source and camera; Bishop et al., 2016), whereas transmissometers are highly collimated but can vary by a factor of 2 in sensitivity based on differences of beam geometry and receiver acceptance angle (Bishop and Wood, 2008; Estapa et al., 2017), (2) effects of particle size distribution on attenuation, (3) wavelength dependence of attenuation (CFE uses the green image plane ($\sim$ 550 nm) vs. (650 nm) red transmissometer) and (4) stray light. Estapa assumed 100 % collection efficiency of particles on the vertically facing transmissometer window and zero contribution of optics biofouling the measurements. The difference in slopes may also be method dependent as Estapa et al. (2017) analyzed only the particulate carbon in 350 μm screened material from the sediment traps, whereas the Bishop et al. (2016) factor includes larger aggregates up to centimeter size.

Given the finding of a factor of 20 for the collection of samples by the surface-tethered OSR, the great uncertainty of literature-based calibration factors, the few environments sampled, and the multitude of lighting and methodological factors affecting the relationship of attenuation and carbon, we needed to develop a particle sampling device that could operate on the CFE. The new integrated system is referred to as "CFE-Cal" (Figs. 1a, A4).
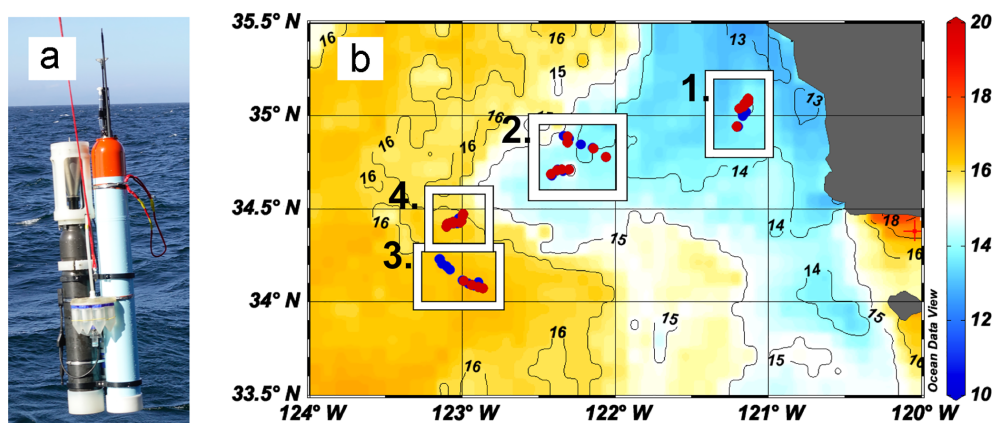
Figure 1. (a) CFE-Cal during deployment from R/V *Revelle* in 2017. The sampling system for particles is interfaced between the optical sedimentation recorder **(a)** and SOLO float **(b)**. **(b)** Map of CFE-Cal deployment and drift locations overlaying map of sea surface temperature (°C) for 10–17 June 2017 from NASA Ocean Color Aqua Modis 4 km resolution (https://oceancolor.gsfc.nasa.gov/, last access: 26 August 2018). Blue dots within location boxes represent CFE-Cal 002 and red dots represent CFE-Cal 004 positions.

Below we describe important design advances that led to the CFE-Cal and report first results from two CFE-Cals that were deployed and recovered 15 times at four locations during the 1 June to 2 July 2017 California Current Ecosystem Long-Term Ecological Research (CCE-LTER) process study cruise aboard R/V *Revelle*. The aim of the CCE-LTER expedition was to characterize food web processes and particle export at different places within and outside of an offshore-flowing phytoplankton-rich filament of upwelled water near Point Conception, CA (Fig. 1b). The diverse environments sampled provided an excellent opportunity to collect a calibration sample dataset under high to low particle flux conditions.

2 Materials and methods

2.1 CFE, CFE-Cal and optical attenuation

Bishop et al. (2016) describe in detail the CFE and the operation of its particle-flux-sensing OSR. These core elements are identical to those of the CFE-Cal. Briefly, once released from the ship the CFE dives repeatedly below the surface to obtain OSR observations at up to three target depths as it drifts with currents. The CFE's OSR awakes when the target depth is reached. Particles settle through a hexagonal celled baffle (1 cm opening) into a high-aspect-ratio funnel (15.4 cm diameter opening) assembly before depositing on a 2.54 cm diameter glass sample stage. Particles are imaged at 13 µm pixel resolution in three lighting modes: transmitted, transmitted–cross polarized and dark field. Here we focus on CFE-Cal results and on the calibration of volume attenuation determined from transmitted light imagery in terms of POC, PN and PP sample loading. This study focuses on the calibration of VA : POC and PN. In future studies, cross-polarized photon yield measured by the CFE, as discussed in Bishop

et al. (2016), will be calibrated in terms of PIC units also using the sampler. As the samples collected on filters had large amounts of residual sea salt, the separation of the non-salt Ca requires very high accuracy and a separate protocol.

On first wake-up of a given CFE dive, the sample stage is flushed with water and images of the particle-free stage are obtained. At timed intervals (~ 25 min in the data described here) the OSR repeats image sets, which register the sequential buildup of particles. The 25 min interval was determined to be consistent with previous CFE studies (Bishop et al., 2016). After a predetermined number of image sets over ~ 1.8 h, stage cleaning occurs and a new reference image set is obtained. After ~ 5–6 h at a target depth, the OSR performs a final image set, cleaning cycle and reference image set, and the CFE surfaces to report GPS position, CTD profile data and OSR engineering data, then it dives to its next target depth. All target depths in this study were chosen to be at 150 m. We describe in detail below the particle sampler and its integration with the CFE to form the CFE-Cal. In the case of the CFE-Cal, stage cleaning operations direct particles from each dive to a unique sample bottle.

Image attenuance was calculated following Bishop et al. (2016). Briefly, transmitted light images were normalized by a composite in situ image of the particle-free sample stage. The $-\log_{10}$ of the normalized image was taken to yield attenuation (ATN) values. Pixels with an ATN value less than 0.02 were defined to be background. Pixels with attenuation values above 0.02, determined to be particles, were integrated across the sample stage then divided by the total number of pixels in the sample stage area to yield average attenuation. This is multiplied by 1000 to yield mATN and then by the sample stage area to give sample volume attenuance (units: mATN cm^2). As light is reduced exponentially as it passes through particles, as long as the overlapping particles do not 100 % obscure the transmitted light, attenuation af-
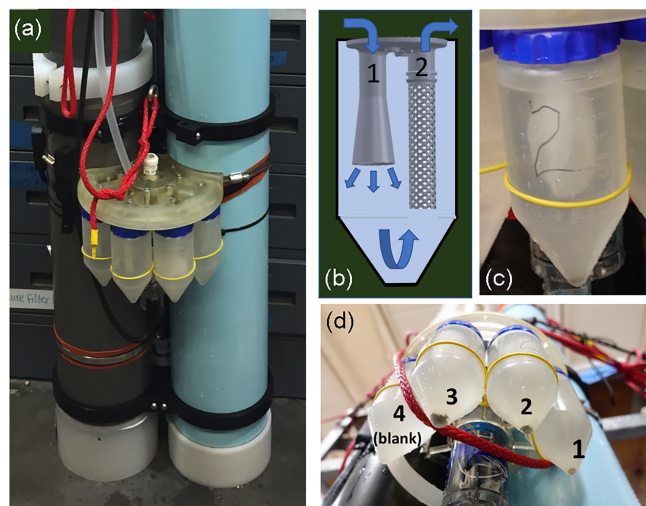
Figure 2. (a) Sampler on CFE-Cal. Suction action of a pump draws water and particles down a poly tube to the sampler (shown disconnected). **(b)** Detail of particle retention system within sample bottles. Inlet is cone shaped to decelerate incoming flow. Outlet is formed to accommodate 51 μm mesh, which is retained by two O-rings at the top. **(c)** Close-up of bottle with mesh filter in place; filter area is ∼ 130 cm^2. **(d)** CFE-Cal recovery after 24 h deployment showing collected samples. Bottle 2 is shown in **(c)**. In this case, bottle 4 was a blank (i.e., no particles directed to it).

fects are additive. In our analysis, the transmitted light, even in the presence of multiple overlaid large aggregates, never went to zero (in other words, attenuation was never saturating). Therefore, overlapping particles are not an issue in this study.

The depth-seeking performance of the CFE-Cal, imaging and sampling times, and derived VA time series are illustrated in Fig. A1 in the Appendix. In order to compare VA to filter loads of POC, PN and PP, the cumulative VA over the course of a dive had to be calculated. The tilt of CFE-Cals during drift is about 3°; the minimization of tilt is required to ensure optimal distribution of particles across the sample stage (Fig. A2). During a dive, particles are transferred from the image stage to a specific sample bottle between two and six times. For each cleaning cycle, the VA of a clean image was subtracted from the image with particles prior to transfer to a bottle. This then represented the amount of material directed into the sample bottle after cleaning. VA from each cleaning step was then summed to yield a cumulative VA, which should correspond exactly to the particles directed into the sample bottle (Table S1 in the Supplement).

2.2 Sampler

Most key components of the sampler for the CFE-Cal were fabricated in the Advanced Prototyping Lab at the Jacobs Institute for Design Innovation at UC Berkeley using a Multi-Material Color Objet260 Connex3 (Stratasys, Israel); some

parts were also fabricated using the carbon model M1 3-D printer (Redwood City, CA). We chose these particular additive manufacturing processes because they were fast, low-cost and enabled improved functional designs that were impossible to machine.

The new sampler incorporates the operation and water flow logic of a sampler built in 2004 for our surface buoy-tethered OSR but improves on it considerably (Fig. 7f in McDonnell et al., 2015; Bishop et al., 2016). The physical layout of the sampler is entirely new as the CFE-Cal had to meet stringent dimensional, buoyancy, compressibility, drag performance and tilt criteria. Furthermore, as the sampler is intended to collect samples for particulate carbon, nitrogen, phosphorous, calcium carbonate, silica and trace metals, it needed to be non-contaminating.

Figure 2a shows details of the integration of the sampler with four mounted sample collection bottles on the CFE-Cal; Fig. 2b and c detail the particle isolation system within each sample bottle. A planetary gear motor (2842S024C; Faulhaber Group, Micromo, Florida) and related custom electronics that actuate the sampler are housed in a pressure-compensated acrylic tube filled with Fluorinert (3M) fluid and mated coaxially with the rotor (Fig. 2d). Fluorinert was selected as it is clear (necessary as there was an optical encoder in the pressure-compensated chamber), low viscosity (for motor immersion) and inert (necessary as there were electronics in the chamber). The optical encoder provides feedback as to the proper location for the desired sampling bottle. Figure A3 shows details of the design of key 3-D-printed elements of the sampler. The sampler inlet is connected to the particle settling stage by a 40 cm long 9.5 mm inner diameter (ID) polyethylene tube (seen in Fig. A3), and its outlet is connected by a second 20 cm polyethylene tube to a SBE model 5T (2000 RPM) pump (Sea-Bird Electronics, WA). Flow rate during cleaning was ∼ 20 mL s^{-1}. When the CFE reaches depth on a new dive, the rotor is moved to select a water path that bypasses the sample bottles (Fig. 2a, port 0) and the flow is directed to the outlet manifold. The bypass cleaning volume is ∼ 800 mL. After a cycle of particle accumulation and imaging, the motor-driven sampler rotator opens to one of four sample bottle positions (1–4, Fig. 2a), and the suction action of the pump draws water and particles from the imaging stage into the selected 250 mL conical clarified polypropylene centrifuge tube (Thermo Scientific). A total of ∼ 400 mL of water is drawn through the sampling system during each regular cleaning cycle and represents about 30 % of the volume of the collection funnel (∼ 1460 cm^3). All particle transfers from a dive are directed to the same bottle (diamond points in Fig. A1). Particles are retained in the bottle by a 14 cm diameter circle of 51 μm polyester 33 % open-area mesh (SEFAR 07-51/33) wrapped and secured using silicone O-rings around the outlet structure within the bottle (Fig. 2c). The area of the perforated outflow cylinder was ∼ 30 cm^2; however, when the circular mesh was secured to the top of the outlet cylinder by an O-

ring, the pleated mesh area exposed to flow was ~ 130 cm^2 (Fig. 2c).

The flow from the imaging stage to the bottle is constricted by the six 3 mm diameter openings that surround the sample stage. Loosely aggregated material is likely distorted or broken up into smaller pieces while being transferred. For cohesive particles (such as siphonophores) and rigid particles (such as some pteropod shells), the upper size limit is 3 mm. Though nothing was caught in the CFE-Cals during this study, there was one case in which a larval crab was caught in one of the profiling CFEs and was not able to fit through the 3 mm diameter opening. This had to be removed after the CFE was retrieved.

2.3 Sampler materials

Little is known about the water absorption properties, dimensional stability, chemical reactivity and contamination potential of the 3-D printing resins as most are proprietary. The majority of sampler parts were fabricated using the Connex3 from FullCure 720 resin (Fig. A3), and some of the particle isolation assemblies were printed in both FullCure 720 and VeroWhite RGD35 resins. The Connex3 is a fused deposition modeling (FDM) printer that builds parts layer by layer. We fabricated three additional particle isolation assemblies from amber cyanate ester, black rigid polyurethane and black polylactic (PLA) resins on the carbon printer; the process uses photopolymerization to form a solid piece as material is drawn from liquid resin. After parts were printed and support material removed, the parts were rinsed with deionized water and then leached in a 1.2 M HCl solution for 16 h at room temperature. All remained stable during this treatment. Dimensional tests before and after sea trials showed that the dimensions of the sampler body (Fig. A2) printed with FullCure 720 remained stable to within 0.06 % of design dimensions.

2.4 Field procedures

Prior to each deployment, the CFE sample stage and related glass surfaces were cleaned to remove any remaining material collected from the previous deployment. Areas between glass layers were flooded with water to prevent air bubbles from being trapped. Each CFE-Cal was outfitted with four clean sample collection tubes and filled with 0.4 µm filtered seawater. On recovery of the CFE-Cals, the sample bottles (Fig. 2d) were either immediately removed from the sampler and filtered or placed in a fridge at 10 °C to minimize sample degradation; in the latter case, samples were processed within 3 h of collection.

All sample processing and manipulation took place in a laminar flow bench at sea. Each sample was decanted into an open filter funnel loaded with either 47 mm diameter Whatman quartz fiber (QMA; pore size ~ 1.2 µm) or Supor (pore size 0.4 µm) filters; transfer took place with filters under mild

suction with the aim of evenly covering the filter surface (Fig. A3). Each sample tube and associated 51 µm mesh were further rinsed three times with ~ 5 mL of 0.4 µm filtered seawater to ensure quantitative transfer of particles. After filtration, the samples were quickly misted with ~ 3 mL of deionized water (DI) to reduce residual sea salt while still under suction. Samples were then placed on Gelman Petri slides and photographed wet under LED ring light illumination using a 20 megapixel Sony RX100 V camera (pixel resolution of 19 µm), dried at 50 °C for 24 h and photographed again under the same lighting conditions in a laminar clean air bench. Dried samples were then stored in covered Petri slides until analyzed in the laboratory. Prior to use, the QMA filters were placed in a muffle furnace at 450 °C overnight to reduce carbon blanks. Both the QMA (after combustion) and the Supor filters were leached in a 1.2 M HCl solution for 24 h at room temperature, rinsed with deionized water and air-dried in a class 100 laminar flow bench prior to use.

2.5 Laboratory procedures

2.5.1 Carbon and nitrogen analysis

Briefly, half of each QMA filter was placed in a desiccator and exposed to HCl fumes (from 12 M HCl) for 24 h to remove any carbonate carbon (Bishop et al., 1978) and then dried at 30 °C for 36 h and subsampled six to eight times using a 3 mm diameter biopsy punch, yielding ~ 1/16th of the whole sample. These were loaded into tin capsules and analyzed for total organic carbon and nitrogen using a Thermo Quest EA2500 elemental analyzer at Oregon State University according to Holser et al. (2011). A total of 27 unique cruise samples and process blanks (with 6 replicates), five unused QMA filters, and analytical blanks (empty tin capsules) were run. Process blanks were samples for which no particles were directed to the sample tube during deployment and processed as other samples. The other half of the sample was preserved for ICP-MS analysis.

Corrected POC was calculated following Eq. (1).

$$POC_{corrected} = POC_{measured} - POC_{process\,blank} \qquad (1)$$

The sample POC error was calculated following Eq. (2).

$$POC_{error} \qquad\qquad\qquad\qquad\qquad\qquad\qquad (2)$$
$$= \sqrt{(process\,blank\,s.d.)^2 + (sample\,RSD \times POC_{corrected})^2}$$

Nitrogen and phosphorous were calculated the same way, replacing POC with PN and PP.

2.5.2 ICP-MS phosphorous analysis

Samples on both Supor and QMA filters were analyzed using a Thermo Fisher Element II XR inductively coupled plasma–mass spectrometer (ICP-MS) at the UC Santa Cruz Marine Analytical Laboratory following Bishop et al. (2012). Half

of each 47 mm filter was leached in 10 mL of a 0.6 M HCl solution at 60 °C for 16 h. The leach solution was then diluted with 18.2 MOhm cm Milli-Q DI water to 50 g; 1 mL of the diluted solution was then further diluted with 3 mL of 0.12 M HCl and spiked with 0.2 mL of 25 ppb In. Standards were prepared in the same acid matrix.

3 Results and discussion

3.1 Samples collected

Samples were collected from four productivity regimes and environmental conditions, yielding a diverse array of particle sizes and classes (Fig. 3a–e). The flux rates between locations also varied widely. At location 1, flux was at times dominated by 1 mm diameter, 5–10 mm long anchovy pellets similar to those described by Saba and Steinberg (2012) with 95 % of VA flux (average $\sim 40\,\mathrm{mATN\,cm^2\,cm^{-2}\,d^{-1}}$) being carried by particles > 1.5 mm in size. In contrast, at location 2, numerous small diameter (200–300 µm) olive-green ovoid pellets dominated imagery and accounted for $\sim 50\,\%$ of the $\sim 15\,\mathrm{mATN\,cm^2\,cm^{-2}\,d^{-1}}$ VA flux. Location 3, in transitional waters near the filament edge, had a VA flux of $\sim 2.3\,\mathrm{mATN\,cm^2\,cm^{-2}\,d^{-1}}$ and $\sim 65\,\%$ of the flux carried by aggregates larger than 1.5 mm. At location 4, in the most extended part of the filament, VA flux was $\sim 22\,\mathrm{mATN\,cm^2\,cm^{-2}\,d^{-1}}$, and 94 % of the flux was carried by aggregates > 1.5 mm in diameter.

The CFE-Cals were new and there were initial malfunctions (i.e., instrument not diving to depth, not stabilizing at depth, or sampler not switching target bottles correctly), which were mostly resolved during the first half of the expedition. In all, the CFE-Cals were deployed 15 times over the course of the June 2017 CCE-LTER study, the CFE was outfitted with four sample bottles for each deployment. For each deployment, depending on how much time was available, the CFE-Cals performed three to four dives. Of these 60 possible sample collections, 10 were not useable due to a CFE-Cal malfunction, and one was not useable due to a swimming organism. Table 1 details all these points as well as noting sampling times, depths and filter type. The CFE-Cal instruments were built using the new SOLO2 floats, whereas the original CFEs were built using SOLO1 floats. We found that the concave bladder housing of the new SOLO2 float design trapped air and made it more difficult for the CFE to attain its target depth. Once we realized this issue, the bottom of the float was flushed with water prior to each deployment and care was taken to launch the float horizontally to prevent this. As all instrument malfunctions were identified and resolved, future deployments will be far more robust.

A total of 15 QMA samples were analyzed for POC and PN; these 15 QMA samples and 19 Supor samples were analyzed for PP. Samples ranged from 0.0267 to 0.1570 mmol C per filter (average ±SD: 0.0760 ± 0.0362) and 0.0029 to
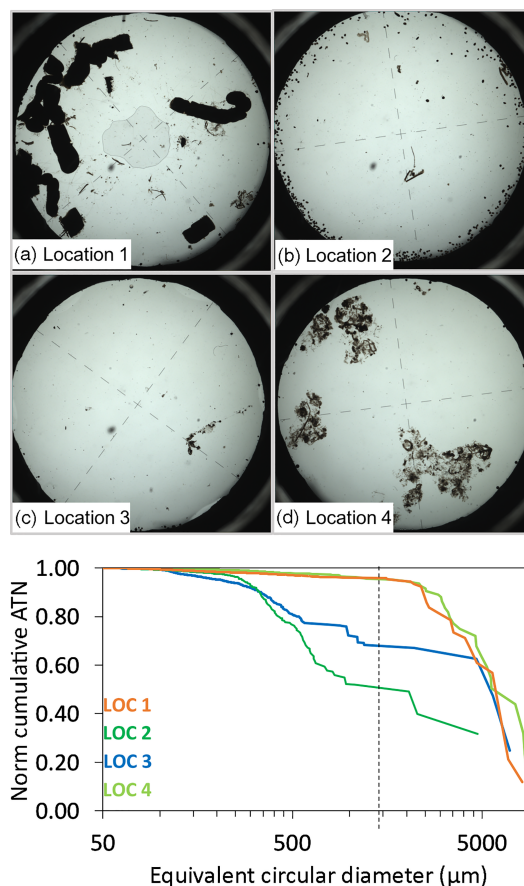
Figure 3. Representative images from four locations. The particle size classes varied widely at the four different locations. **(a)** In location 1, flux was dominated by large 1 mm diameter anchovy fecal pellets. **(b)** Flux was dominated by small ovoid pellets 200–300 microns in diameter. **(c)** Location 3 was characterized by very low flux. Flux was dominated by small particles with the occasional large aggregate. **(d)** Flux was dominated by large aggregates. **(e)** Cumulative normalized volume attenuance vs. equivalent circular diameter curves representative of the four locations. Approximately 95 % of flux was carried by aggregates > 1.5 mm in size at locations 1 and 4. Location 2 had $\sim 50\,\%$ of flux in the > 1.5 mm fraction.

0.0155 mmol N per filter (average ±SD: 0.0065 ± 0.0034). Phosphorous in samples ranged 40-fold from 3.9×10^{-5} to 1.5×10^{-3} mmol P per filter (average ±SD: 2.0×10^{-4} $\pm 2.4 \times 10^{-4}$). Results are shown in Table S1.

Process blanks were subtracted from the sample values as shown in Eq. (1). As there were only five QMA process blanks, an average of the five was used to blank correct POC and PN. This drove one POC and one PN sample from location 3 negative, though not negative within error. Fluxes at location 3 were very low – an order of magnitude lower than samples collected in other regions. Process blanks contained 0.032 ± 0.008 mmol C per filter and 0.003 ± 0.0003 mmol N per filter. Unused QMA blanks were 0.0037 ± 0.0008 mmol C per filter and were below the detection limit for nitrogen;

Table 1. CFE-Cal 2017 deployments during the California Current Ecosystem Long-Term Ecological Research process study. This table notes the location number, CFE number, longitude and latitude position, dive number, bottle number, filter type, sampling interval and depth interval of sampling. Filters marked with the * symbol are process blanks. The note column indicates any sample notes, including any instrument malfunctions. UTC day: days since 00:00 on 1 January; noon on 1 January: UTC day 0.5.

Study loc.	CFE	Latitude (° N)	Longitude (° W)	Dive	Bottle	Filter	UTC day start	UTC day end	Hours	Depth (m)	Depth SD	Sample notes
1	2	35.0739	121.1281	40	1	Supor	160.064	160.270	4.944	0.2		CFE-Cal did not dive
1	2			41	2	QMA	160.333	160.500	4.008	70.0	12.3	
1	2			42	3	Supor	160.623	160.791	4.032	119.4	7.8	not analyzed
1	2	34.9978	121.1650	43	4	QMA*	160.849	160.851	0.048	186.0		
1	4	35.0885	121.1293	40	1	QMA	160.076					selector failure
1	4			41	2	Supor	160.297					selector failure
1	4			42	3	QMA	160.422					selector failure
1	4	35.0341	121.1862	43	4	Supor	160.732					selector failure
1	2	34.9396	121.2031	50	1	QMA	162.091	162.294	4.872	131.7	10.9	
1	2			51	2	Supor	162.424	162.536	2.688	31.8	4.4	not analyzed
1	2				3	QMA*						
1	2	34.8962	121.2032		4	Supor*						
1	4	34.9348	121.1946	50	1	Supor	162.075	162.280	4.908	189.5	7.7	oil under sample stage
1	4			51	2	QMA	162.410	162.412	0.048	286.2		depth unstable
1	4			52	3	Supor	162.549	162.551	0.048			depth unstable
1	4	34.8997	121.2165		4	QMA*						
2	2	34.7771	122.0572	60	1	Supor	165.047	165.264	5.208	142.9	3.8	
2	2			61	2	Supor	165.406	165.574	4.032	112.8	4.3	
2	2			62	3	Supor	165.716	165.883	4.008	97.7	4.1	
2	2	34.8651	122.3355		4	QMA	166.024	166.026	0.048			surfaced open at position 4
2	4	34.7742	122.0587	60	1	QMA	165.060	165.278	5.232	160.9	4.2	C/N > 20
2	4			61	2	Supor	165.430	165.597	4.008	153.1	5.7	not analyzed
2	4			62	3	QMA	165.739	165.900	3.864	150.2	3.0	
2	4	34.8825	122.3499		4	Supor*						
2	2	34.7098	122.3004	70	1	Supor	166.659	166.882	5.352	159.2	5.1	
2	2			71	2	QMA	167.034	167.202	4.032	146.2	5.8	
2	2			72	3	Supor	167.350	167.517	4.008	147.8	3.9	
2	2	34.6771	122.4122		4	QMA*						
2	4	34.7091	122.2998	70	1	QMA	166.673	166.897	5.376	164.2	10.3	
2	4			71	2	Supor	167.044	167.211	4.008	157.6	3.4	
2	4			72	3	QMA	167.364	167.531	4.008	151.5	2.9	C/N > 20
2	4	34.6829	122.4185		4	Supor*						
3	2	34.2275	123.1480	80	1	QMA	170.192	170.368	4.224	141.5	6.7	
3	2			81	2	Supor	170.472	170.639	4.008	131.4	3.8	
3	2			82	3	QMA	170.740	170.879	3.336	143.7	6.7	C/N > 20
3	2	34.1717	123.0758		4	Supor*						
3	4	34.1129	122.9885	90	1	QMA	171.205	171.414	5.016	173.4	3.3	
3	4			91	2	Supor	171.553	171.721	4.032	160.9	0.1	
3	4			92	3	QMA	171.860	171.903	1.032	148.8	0.8	
3	4	34.0749	122.8673		4	Supor*						
3	2	34.1086	122.9823	90	1	Supor	171.190	171.369	4.296	126.9	4.8	
3	2			91	2	QMA	171.468	171.636	4.032	159.7	5.7	
3	2			92	3	Supor	171.737	171.904	4.008	154.7	3.6	
3	2	34.0714	122.8552		4	QMA*						
4	4	34.4070	123.0958	100	1	Supor	174.180	174.369	4.536	190.6	5.7	
4	4			101	2	Supor	174.489	174.657	4.032	117.3	3.3	
4	4			102	3	Supor	174.767	174.899	3.168	135.0	3.5	
4	4	34.4174	123.0535		4	Supor*						

Table 1. Continued.

Study loc.	CFE	Latitude (° N)	Longitude (° W)	Dive	Bottle	Filter	UTC day start	UTC day end	Hours	Depth (m)	Depth SD	Sample notes
4	2	34.4032	123.0964	100	1	QMA	174.294	174.354	1.440	165.8	132.5	depth unstable
4	2			101	2	Supor	174.479	174.646	4.008	139.9	3.0	
4	2			102	3	QMA	174.742	174.903	3.864	129.5		
4	2	34.4216	123.0310		4	Supor*						
4	4	34.4221	123.0133	110	1	QMA	175.187	175.487	7.200	164.0	5.4	
4	4			111	2	Supor	175.599	175.878	6.696	101.7	3.7	
4	4			112	3	QMA	175.989	176.267	6.672	158.6	3.9	
4	4	34.4449	123.0205	113	4	Supor	176.396	176.496	2.400	119.8	1.8	
4	2	34.4218	123.0168	110	1	Supor	175.173	175.469	7.104	162.8	5.5	
4	2			111	2	QMA	175.582	175.859	6.648	159.5	3.4	swimming siphonophore
4	2			112	3	Supor	175.965	176.242	6.648	156.9	3.0	
4	2	34.4335	123.1008	113	4	Supor	176.350	176.516	3.984	153.1	2.3	

only 12 % of carbon in the process blanks came from the blank filter. Nearly 90 % of the process blank carbon is therefore not from the blank filter, but stems from either accidental collection of particles during deployment or contamination during processing. Particles may be accidentally collected by entering a sample bottle while the sampler is turning and the selector briefly passes the blank bottle inlet.

As there were at least two process blanks per location for PP, blanks could be location specific. The process blanks were 8.9×10^{-5}, 5.0×10^{-5}, 1.9×10^{-5} and 5.0×10^{-5} mmol P per filter for locations 1, 2, 3 and 4, respectively.

Replicate analysis of four samples gave an average relative standard deviation (RSD) of 0.14 and 0.07 for C and N, respectively. Punched subsamples are collected evenly distributed across the filter, but inevitably as there are discrete particles on the filter, there is some heterogeneity between the subsamples (Fig. 5a). The RSD of replicate analysis we assume is attributed to this sample heterogeneity and can be applied to all samples. The RSD for replicate analyses of process blanks was 0.18 and 0.12 for C and N, respectively.

3.2 Transfer efficiency

To validate the efficiency of the transfer of particles imaged to sample bottles, ovoid pellets (200–300 µm) were manually counted (Fig. 4) in both the CFE's OSR images and photographs of filters of material sampled at location 2. CFE-Cal2 collected close to the same number of particles in the sampler as were imaged (on average, there was less than a 9 % difference between particles imaged and particles filtered; particles were not exclusively higher in one or the other). CFE-Cal4, however, collected 1.45 times more ovoid pellets in the sampler than were imaged. The sampler uses an optical encoder to sense a home position from which it advances to select specific bottles. Software is programmed with a time-out in the case that the "home" position cannot be found to prevent continuous operation and depletion of
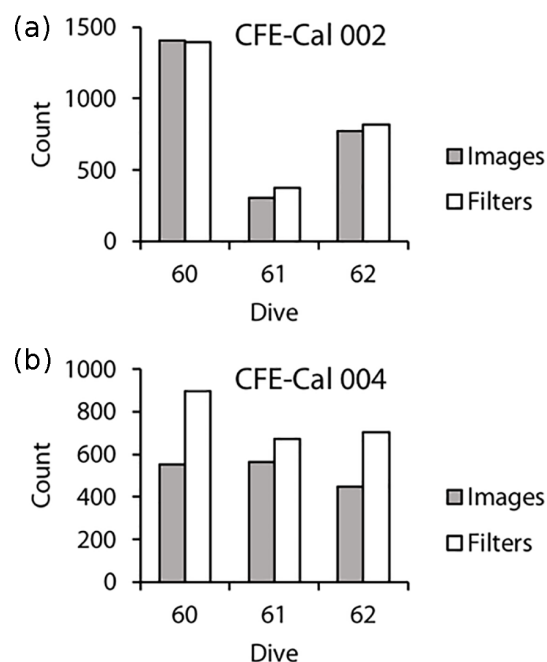
Figure 4. Comparison counts of ovoid pellets in images vs. on filters. **(a)** CFE-CAL002 deployment 3 (first deployment at location 2), **(b)** CFE-CAL004 deployment 4 (second deployment at location 2).

the CFE batteries. During pre-cruise tests of the CFE-Cal no positioning errors were registered. However, these tests were done in a lab, with room-temperature fresh water and not in 10 °C seawater under pressure. It is clear that the sampler for CFE-Cal4 stopped short of the home position, and this likely led to the over-transfer of particles that were not imaged. We recognized this issue during deployment operations at cycle 3 and after the time-out limit was adjusted; this problem was not encountered again. The known sampler positioning issues at this time may have led to the transfer of
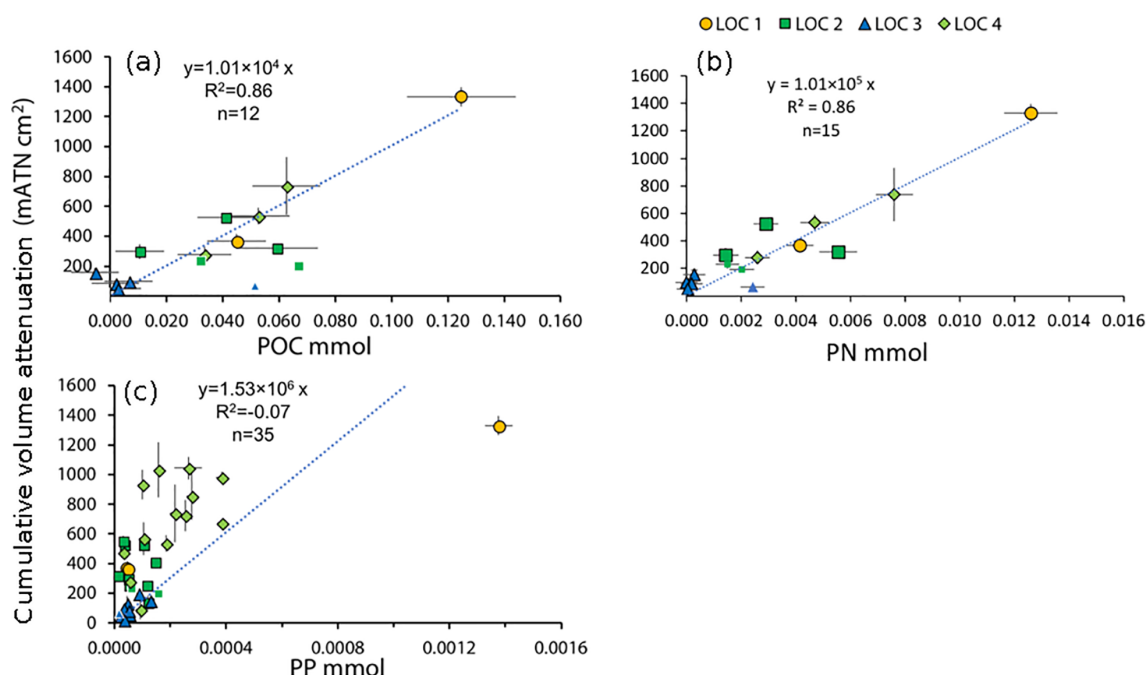
Figure 5. Data and regressions of sample POC **(a)**, PN **(b)** and PP **(c)** vs. cumulative volume attenuance. Fits are forced through zero. Smaller symbols in all plots denote samples excluded from the POC regression analysis; these had C/N values > 20 and were likely contaminated for carbon and not nitrogen. No data were excluded from PN or PP regressions.

pellets to bottles from times (such as during float ascent to the surface) when particles were not imaged by CFE-Cal4. To correct for this, the POC, PN and PP numbers for CFE-Cal4 at locations 1, 2 and 3 were divided by 1.45.

Bishop et al. (2012) investigated the effect of filtration rate on aggregate retention during large-volume in situ filtration sampling and found that aggregates were broken up when the flow velocity through 51 μm mesh exceeded $1\,\mathrm{cm\,s^{-1}}$ over a 4 h sampling time. During CFE-Cal stage cleaning, the sample transfer pump is operated for two cycles of 10 s at a flow rate of $\sim 20\,\mathrm{mL\,s^{-1}}$. The mesh area on the outflow from the sample bottle is approximately $130\,\mathrm{cm^2}$. We thus calculate the flow speed through the mesh to be $\sim 0.15\,\mathrm{cm\,s^{-1}}$, 15 % of the threshold speed recommendation by Bishop et al. (2012). Although intact large aggregates were not seen on the sample filters (compare Fig. A3d vs. Fig. 3d), given our limited sample transfer time (< 2 min) and low flow velocity, we believe that our transfer efficiency for the particles comprising the loosely aggregated material is similar to that for the more robust pellets.

3.3 Calibration results

Figure 5 shows cumulative VA regressed against sample POC, PN and PP (data in Table S1). All of our results are forced through zero as both VA and elemental values are blank controlled. Regression results yielded slopes, R^2 values and numbers of samples (in parentheses) of $1.01 \times 10^4\,\mathrm{mATN\,cm^2}$: mmol POC ($r^2 = 0.86$, $n = 12$, $p < 0.001$)

and $1.01 \times 10^5\,\mathrm{mATN\,cm^2}$: mmol PN ($r^2 = 0.86$, $n = 15$, $p < 0.001$). Three of 15 samples had C/N ratios above 20 and were not used in the regression for POC as these numbers are not typical of sinking particles (e.g., Bishop et al., 1977; Lamborg et al., 2008; Stukel et al., 2013). Stukel et al. (2013) reported trap POC/PN mole ratios ranging from 5 to 14 (average, 9.6) at 100 m in the same upwelling regime we have sampled; Lamborg et al. (2008) reported POC/PN ratios ranging from 7.7 to 8.5 in productive waters of the Oyashio and oligotrophic waters of the North Pacific Gyre. The molar ratio of 10 C/N from our regression slopes is in line with Stukel et al. (2013).

The high C/N values of excluded samples may have been due to contamination by residual material used as a scaffold to build the 3-D-printed parts; in one case, a 1 mm sized aggregate of such material was found on our filters. New lighting systems were rapidly prototyped just prior to the cruise. The scaffold material, Stratasys OBJET Support SUP706, is made of 1,2-propylene glycol and polyethylene glycol methanone (1-hydroxycyclohexyl) phenyl, both of which contain carbon but not nitrogen (https://store.stratasys. com/medias, last access: 17 March 2019). The material also contains an unspecified acrylic. As the 3-D-printed material contains no nitrogen, C/N values would be elevated if they were contaminated. Including the three high C/N ratio points in the VA : POC regression reduces the slope to 0.86×10^4 with an R^2 of 0.64 ($n = 15$, $p < 0.001$); we report this even

though we do not believe this to be representative of natural particulate.

The data also demonstrate that there is no obvious difference for VA : PN or VA : POC for samples collected from locations 1 and 4 (Figs. 1, 4) where aggregates > 1.5 mm in size accounted for 95 % of the flux compared to locations 2 and 3 where smaller material contributed 50 % and 30 % of the flux, respectively.

The relationship for VA : PP was scattered with a slope of 1.53×10^6 mATN cm² : mmol PP ($R^2 = -0.07$; negative R^2 values denote results worse than horizontal fit). The sample with anchovy fecal pellets had a POC : PP ratio of 90 mol mol^{-1}, far lower than all other samples (∼ 300 mol mol^{-1}). The fact that PP had zero correlation with VA is consistent with the strong loss of P relative to carbon and nitrogen as large aggregates sink (e.g., Bishop, 1977; Lam et al., 2007). Scanning electron microscopy showed that the anchovy fecal pellets were stuffed with diatoms and as they are larger and sink at a much faster rate (up to 500 m d^{-1}), it follows that this sample should have a higher PP content as there is less time for microbial degradation and remineralization. When this point is arbitrarily removed, the relationship of VA : PP for non-anchovy aggregates improved 3.23×10^6 mATN cm² : mmol PP ($R^2 = 0.41$). Though the ultimate goal is to allow for an estimation of biogeochemical fluxes based on image analysis, because of the known lability of PP relative to POC or PN in sinking particles, we conclude that PP cannot be predicted from VA.

As mentioned earlier, we found that CFE-Cal4 collected 1.45 times more ovoid pellets on the filters than were imaged due to a sampling issue, and we therefore divided the CFE-Cal4 POC and PN samples for locations 1, 2 and 3 by this empirically derived factor. This affected six samples in the POC and PN regressions (see Table S1). We note that if instead of applying this empirical factor, these samples are removed from the regression, the VA : POC and VA : PN slopes both change less than 5 %. The slopes (number of samples and R^2 in parentheses) change to 1.06×10^4 ($n = 8$, $R^2 = 0.93$) and 1.04×10^5 ($n = 9$, $R^2 = 0.91$). Using these data, which have been corrected using the empirical factor, therefore affects the overall regression very little.

3.4 Comparison to previous studies

Two autonomous flux monitoring systems, the CFE (Bishop et al., 2016) and the OST (Estapa et al., 2017), have now been calibrated to relate the attenuation flux to the flux of particulate organic carbon. This study expands upon Estapa et al. (2017) as samples from a wide range of environments and with a far greater range of aggregate size distributions have been collected. The highest POC flux collected for the Estapa et al. (2017) calibration was under 2 mmol C m^{-2} d^{-1}. The flux environments sampled in our study ranged from < 2 to 40 mmol C m^{-2} d^{-1}.

Figure 6 compares the relationship between VA flux and carbon flux from this study (data for regression in Table S1) vs. data from Estapa et al. (2017). When converted to compatible units, the slope for the Estapa VA flux (mATN cm² cm^{-2} d^{-1}) vs. POC flux (mmol C m^{-2} d^{-1}) is 1.50 (allowing for an intercept) and 2.19 (forced through zero), while our slope is 1.03 (forced through zero). Estapa et al. (2017) calculate attenuation by taking the natural log of transmittance, and observations are reported in units of ATN m² m^{-2} d^{-1}. Our data are the log$_{10}$ of transmittance as documented in Bishop et al. (2016) and reported in units of mATN cm² cm^{-2} d^{-1}. Therefore, the Estapa published data have been divided by 2.303 to convert the natural log attenuation to log$_{10}$ attenuation and multiplied by 1000 to scale to mATN units. The dimensional data do not require scaling. Our observations were for depths near 150 m and it is unknown if there is a depth dependence to calibration factors. We note that Estapa et al. (2017) combined samples from ∼ 150, 300 and 500 m in the regression. This said, the slopes of our two datasets differ by a factor of 1.5 to 2. In our data, the attenuation of particles in the red image plane is 6 % lower than in green, and thus the wavelength of analysis is a minor factor explaining the differences. Given the large range in particle size distributions and classes (e.g., samples dominated by dense anchovy pellets vs. 2–3 mm size amorphous semitransparent aggregates), we can rule out particle size effects. Beam geometry and the other factors underlying our different methodologies likely explain the differences found.

As noted earlier, Bishop et al. (2016) estimated the factor for conversion of POC flux (C mmol m^{-2} d^{-1}) to VA flux (mATN cm² cm^{-2} d^{-1}) using two previously published values of the carbon-to-particle-volume ratio, as there were no calibration samples available. The two methods are described briefly. In the first method, Bishop et al. (2016) calculated an aggregate volume of 0.113 cm³ for particles > 800 µm (which accounted for 97 % of VA) in a series of five images. An aggregate density of 0.087 g cm³ and 60 % organic matter of dry weight was assumed based on Bishop et al. (1978). To convert the organic matter weight to carbon, a conversion factor of 1.88 was used from Hedges et al. (2002). Using these values yielded an estimated flux of 183 mmol C m^{-2} d^{-1} compared to a VA flux of 66.2 mATN cm² cm^{-2} d^{-1}, which gives a POC flux (C mmol m^{-2} d^{-1}) to VA flux (mATN cm² cm^{-2} d^{-1}) of 2.8 (183 : 6.2 × 0.97 = 2.8). For comparison, POC was also estimated following the methods of Alldredge (1998). Alldredge (1998) derived a regression formula relating the equivalent spherical volume (ESV) and POC content of particles:

$$POC_{\mu g} = 0.99 \times ESV^{0.52}.$$

The Alldredge (1998) relationship has previously been used to estimate carbon content from aggregates in gel trap imagery (Ebersbach and Trull, 2008; Ebersbach et al., 2011) and aggregates collected and then imaged using marine snow
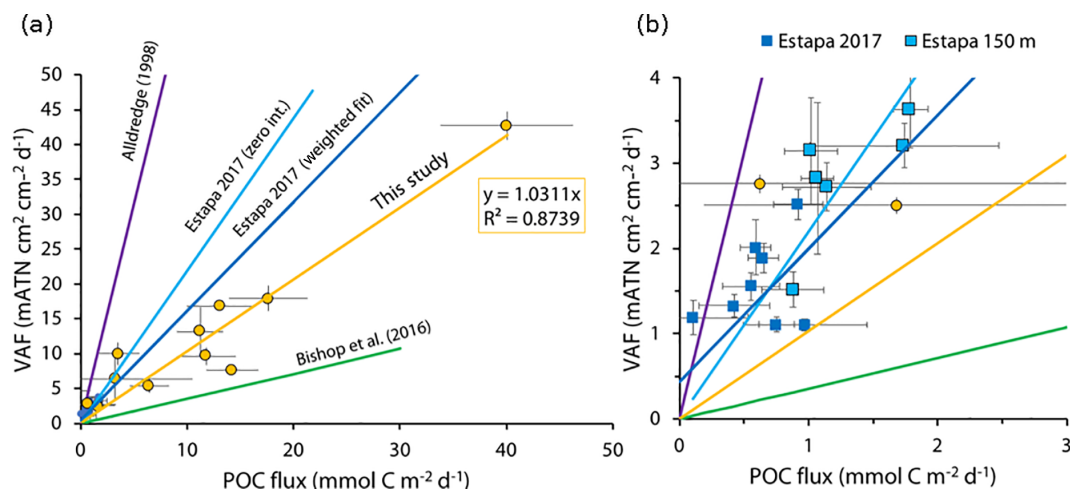
Figure 6. Regressions of volume attenuance flux (mATN cm^2 cm^{-2} d^{-1}) to POC (mmol C m^2 d^{-1}) for this study (orange points and line; $y = 1.03x$, $R^2 = 0.874$) and Estapa et al. (2017, dark blue, weighted fit: $y = 1.56x + 0.434$, $R^2 = 0.632$; light blue line, $y = 2.191x$, $R^2 = 0.47$). The Bishop et al. (2016) estimated slope (green line) is $y = 0.357x$ (1.0/2.8). The Alldredge (1998) estimated slope (purple line) is $y = 6.25x$. As this study's calibration is created using samples collected at 150 m, we separate out the Estapa (2017) data points collected at 150 m by marking them in light blue for comparison. **(a)** The entire range of VAF and POC flux from this study. **(b)** Expanded graph near the origin ($x < 3$ mmol C m^{-2} d^{-1}) showing the range of Estapa et al. (2017) data.

catchers (Riley et al., 2012; Baker et al., 2017). In the Bishop et al. (2016) study, the POC density of aggregates was 0.028 g C cm^{-3} following the first method and 0.0002 g C cm^{-3} using the Alldredge (1998) formula. The 2 orders of magnitude difference was likely due to the fact that the relationship between aggregate volume to POC for Alldredge (1998) was based on aggregates collected at 10–20 m and photographed in situ in, whereas the Bishop et al. (2016) method was based on published values of large particles collected using large-volume filtration between 100 and 400 m of depth. The conversion factor for POC : VAF for Alldredge was 17 times lower than the factor of 2.8 by Bishop et al. (2016). Analysis of directly imaged and sampled material in this study yielded a slope of 1.03 for VAF : POC, which is about 3 times higher than estimated using Bishop et al. (1978) but 6 times lower than inferred from Alldredge et al. (1998) (Fig. 6). It is not surprising that our results are not consistent with Alldredge (1998) as our samples were collected more than 100 m deeper and the Alldredge volumes were calculated based on images taken in situ parallel to the aggregate sinking direction, whereas the CFE images are collected looking upwards after the aggregates have settled onto the glass stage. Though the settling motion is gentle and does not break apart the aggregate, there is very likely some compaction as the particle settles onto the stage.

Bishop et al. (2016) reported CFE attenuation fluxes averaging 66.2 mATN cm^2 cm^{-2} d^{-1} at 150 m in the Santa Cruz Basin in January 2013 and estimated a POC flux of 190 mmol C m^{-2} d^{-1}, about 8 times higher than the highest previously measured flux from surface-tethered sediment traps deployed over a 3-year period at 100 and 200 m, in nearby waters
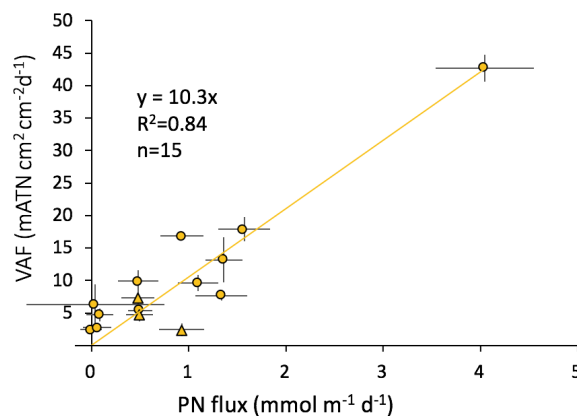
Figure 7. Regressions of volume attenuance flux (mATN cm^2 cm^{-2} d^{-1}) to PN (mmol N m^2 d^{-1}).

(Thunell, 1998; August 1993 to September 1996). Converting the 66.2 mATN cm^2 cm^{-2} d^{-1} attenuation flux to POC flux using our new calibration yields 64.3 mmol C m^{-2} d^{-1}, a value still 3 times higher than the highest previously measured flux (Thunell, 1998). In short, the likely discrimination of surface-tethered baffled sediment traps against the collection of > 1 mm sized particles remains an issue in biologically dynamic regimes dominated by large aggregates. Figure 7 compares the relationship of VAF to particulate nitrogen flux.

4 Conclusions and future development

We have presented the initial calibration of the CFE optical proxy for particulate carbon and nitrogen using the newly developed CFE-Cal instruments. The development of a sampling system for the Carbon Flux Explorer has overcome a major barrier to the calibration of our attenuation proxy for organic matter export. The calibration of volume attenuance flux against organic carbon and nitrogen flux in this study represents an important step forward in the development of autonomous optical flux measurements. Our regression results yield well-correlated calibrations for POC and PN (POC $R^2 = 0.86$, $n = 12$, $p < 0.001$ and PN $R^2 = 0.86$, $n = 15$, $p < 0.001$) that apply over a wide range of environments, including high flux environments in recently upwelled water as well as low flux offshore transitional waters. Phosphorus was shown to be poorly correlated, consistent with the highly labile nature of this element relative to either C or N. Our results give us confidence that images collected by the CFE can be used to calculate the fluxes of carbon and nitrogen. We find less than a two-fold difference in the POC flux vs. volume attenuance flux regression slope from Estapa et al. (2017). This is remarkable given the strongly different environments, methodology and means by which fluxes were sampled. Both these studies reinforce the theory that light attenuation can be used as a proxy for POC and in our case PN flux.

Optimization of CFE-Cal sample return, performance validation and simplification of recovery logistics during CCE-LTER required that all samples in this dataset be collected near 150 m. These calibration samples were all collected off the coast of California during the month of June near 150 m. To make the calibration more robust and determine whether the calibration relationships derived here are widely applicable, it is essential to extend these results to greater depths and to different oceanic regions, environments and ecosystem structures. Intercalibration of the CFE attenuation measurements with other autonomous systems should be pursued.

The results presented above demonstrate that the magnitude of flux and food web processes responsible for flux can vary strongly over relatively small spatial and temporal scales in dynamic coastal waters. Thus, the use of high-frequency autonomous observations will significantly better inform food web and carbon export simulations. Our promising initial calibration of VAF in terms of POC and PN fluxes justifies the further development of instruments that optically measure POC such as the Carbon Flux Explorer.
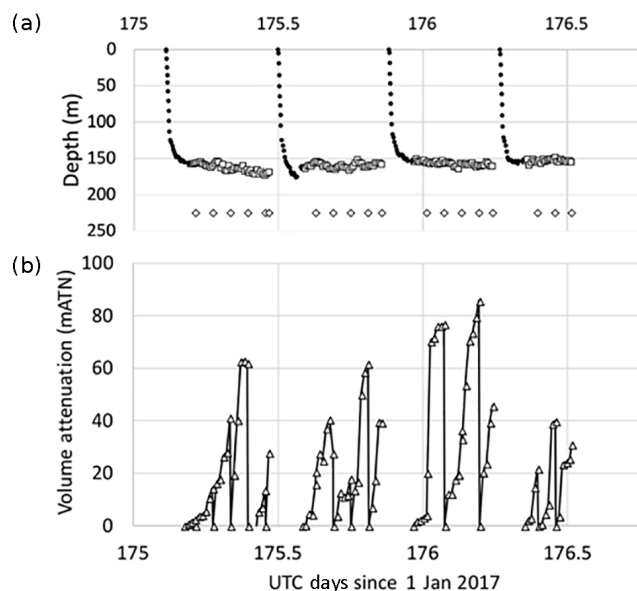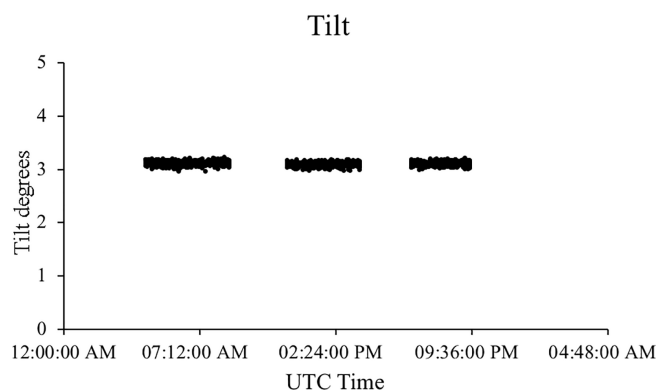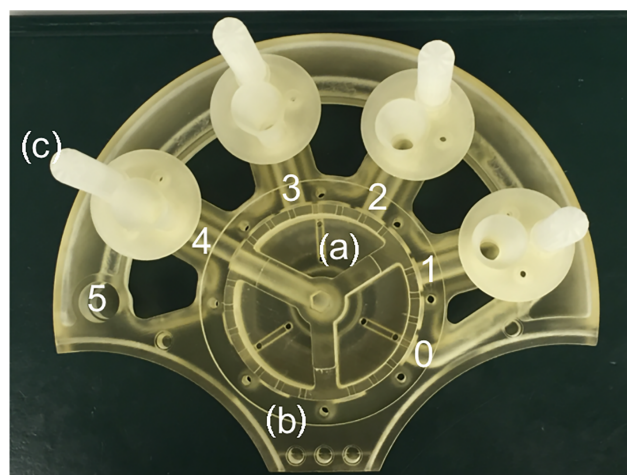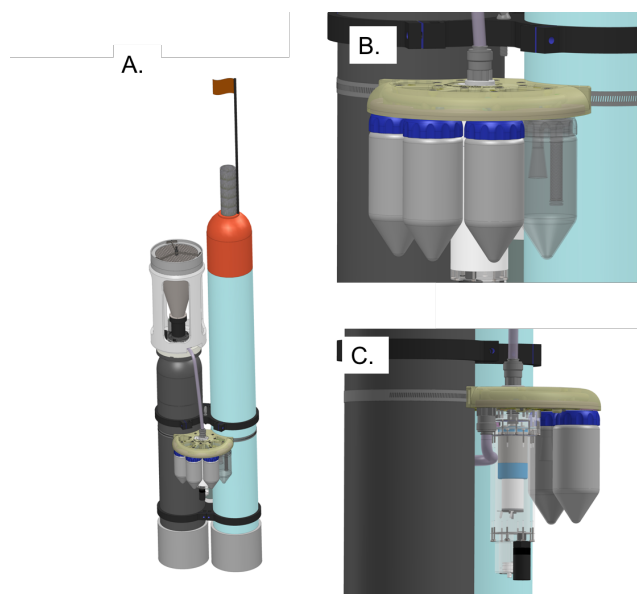
Appendix A

Figure Appendix A1. (a) Typical deployment trajectory of a CFE-Cal. This particular deployment is from CFE2, the first deployment at location 4. The *x* axis is time in days (1 January 2017 at 12:00 UTC = day 0.5). The filled black circles are depths as the CFE-Cal is diving, open black squares denote depths as the CFE drifts and takes images of settled particles. The open black diamonds represent times when the sample stage was cleaned and particles were directed into a sample bottle. **(b)** The corresponding attenuation for each photo taken. Particles build up over time and then periodically the glass stage will be rinsed off and particles directed into the sample bottles. Due to a programming error, the sampler and particles are not removed from the stage.

Figure Appendix A2. Time series of instrument tilt over the course of a deployment. Data are from the CFE-Cal 004 first deployment at location 4. Tilt averages about 3°, consistent with tilt reported for CFEs in Bishop et al. (2016).

Figure Appendix A3. Sampler elements: **(a)** sample selector rotator; **(b)** main structural element of the sampler. Flow paths (1–4) direct water and particles into sample bottles or (0) to bypass sample bottles; **(c)** particle retention system, which bridges inflow channels and common exhaust manifold channel (5). Sample rotator is shown open at position 4. When not sampling, the rotator is sealed to closed positions.

Figure Appendix A4. CFE-Cal configuration. **(a)** The CFE-OSR is on the left and the SOLO2 float is shown on the right. The funnel at the top of the CFE-OSR is covered by hexagonal baffling with 1 cm openings. The funnel is 15.4 cm in diameter. At the base of the funnel is a 2.54 cm diameter glass stage. From here, samples are flushed through the grey tubing pictured above into the sampling unit. **(b)** Close-up of attached sampling system. Far right bottle translucent to show details of bottle inlet and outlet. **(c)** Side view of sampler with one of the bottles removed to show how motor housing is attached to the sampler. The planetary gear motor is located inside the clear acrylic housing.
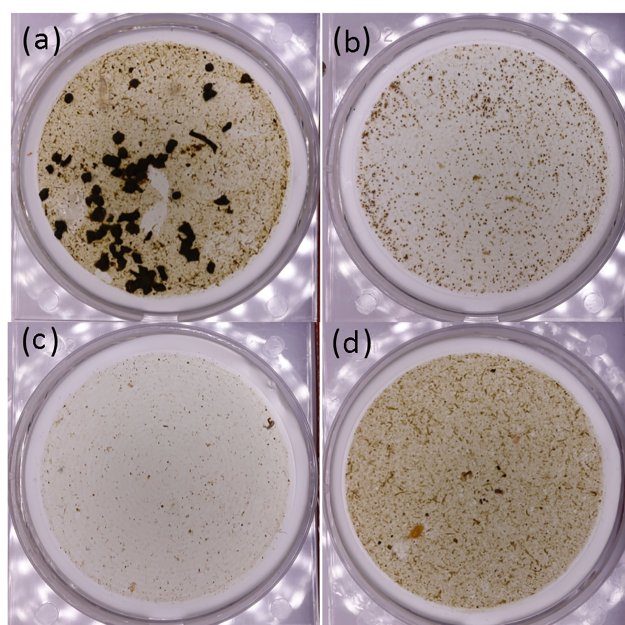
Figure Appendix A5. Representative images of sampled particulate from locations 1–4. The process of sampling retains the morphology of cohesive aggregates. Turbulence on transit from imaging stage to bottle disrupts the integrity of loosely aggregated millimeter-sized particles, as represented in Fig. 3d. **(a)** Location 1. CFE 002 dive 42 – days 160.623 to 160.791 – depth 119.4 ± 7.8 m. **(b)** Location 2. CFE 004 dive 71 – days 167.034 to 167.202 – depth 157.6 ± 3.4 m. **(c)** CFE 002 dive 90 – days 171.190 to 171.369 – depth 126.9 ± 4.8 m. **(d)**. Location 4. CFE 002 dive 101 – days 174.479 to 174.646 – depth 139.9 ± 3.0 m.

References

Alldredge, A. L.: The carbon, nitrogen and mass content of marine snow as a function of aggregate size, Deep-Sea Res. Pt. I, 45, 529–541, https://doi.org/10.1016/S0967-0637(97)00048-4, 1998.

Baker, C. A., Henson, S. A., Cavan, E. L., Giering, S. L. C., Yool, A., Gehlen M., Belcher, A., Riley, J. S., Smith, H. E. K., and Sanders, R.: Slow-sinking particulate organic carbon in the Atlantic Ocean: Magnitude, flux, and potential controls, Global Biogeochem. Cy., 31, 1051–1065, https://doi.org/10.1002/2017GB005638, 2017.

Banse, K.: Reflections About Chance in My Career, and on the Top-Down Regulated World, Annu. Rev. Mar. Sci., 5, 1–19, https://doi.org/10.1146/annurev-marine-121211-172359, 2013.

Bishop, J. K. B. and Wood, T. J.: Particulate matter chemistry and dynamics in the twilight zone at VERTIGO ALOHA and K2 sites, Deep-Sea Res. Pt. I, 55, 1684–1706, https://doi.org/10.1016/j.dsr.2008.07.012, 2008.

Bishop, J. K. B. and Wood, T. J.: Year-round observations of carbon biomass and flux variability in the Southern Ocean, Global Biogeochem. Cy., 23, 1–12, https://doi.org/10.1029/2008GB003206, 2009.

Bishop, J. K. B., Edmond, J. M., Ketten, D. R., Bacon, M. P., and Silker, W. B.: The chemistry biology and vertical flux of particulate matter from the upper 400 m of the equatorial Atlantic Ocean, Deep-Sea Res., 24, 511–548, 1977.

Bishop, J. K. B., Ketten, D. R., and Edmond, J. M.: The chemistry, biology and vertical flux of particulate matter from the upper 400 m of the Cape Basin in the southeast Atlantic Ocean, Deep-Sea Res., 25, 1121–1161, https://doi.org/10.1016/0146-6291(78)90010-3, 1978.

Bishop J. K. B., Calvert S., and Soon, M. Y. S.: Spatial and temporal variability of POC in the northeast subarctic Pacific, Deep. Res. Pt. II, 46, 2699–2733, https://doi.org/10.1016/S0967-0645(99)00081-8, 1999.

Bishop, J. K. B., Davis, R. E., and Sherman, J. T.: Robotic observations of dust storm enhancement of carbon biomass in the North Pacific, Science, 298, 817–821, https://doi.org/10.1126/science.1074961, 2002.

Bishop, J. K. B., Wood, T. J., Davis, R. E., and Sherman, J. T.: Robotic observations of enhanced carbon biomass and export at 55 degrees during SOFeX, Science, 304, 417–420, https://doi.org/10.1126/science.1087717, 2004.

Bishop, J. K. B., Lam, P. J., and Wood, T. J.: Getting good particles: Accurate sampling of particles by large volume in-situ filtration, Limnol. Oceanogr. Method., 10, 681–710, https://doi.org/10.4319/lom.2012.10.681, 2012.

Bishop, J. K. B., Fong, M. B., and Wood, T. J.: Robotic observations of high wintertime carbon export in California coastal waters, Biogeosciences, 13, 3109–3129, https://doi.org/10.5194/bg-13-3109-2016, 2016.

Boss, E., Guidi, L., Richardson, M. J., Stemmann, L., Gardner, W., Bishop, J. K. B., Anderson, R. F., and Sherrell, R. M.: Optical techniques for remote and in-situ characterization of particles pertinent to GEOTRACES, Prog. Oceanogr., 133, 43–54, https://doi.org/10.1016/j.pocean.2014.09.007, 2015.

Briggs, N., Perry, M. J., Cetinić, I., Lee, C., D'Asaro, E., Gray, A. M., and Rehm, E.: High-resolution observations of aggregate flux during a sub-polar North Atlantic spring bloom, Deep-Sea Res. Pt. I, 58, 1031–1039, https://doi.org/10.1016/j.dsr.2011.07.007, 2011.

Buessler, K. O., Antia, A. N., Chen, M., Fowler, S. W., Gardner, W. D., Gustafsson, O., Harada, K., Michaels, A. F., Rutgers van der Loeff, M., Sarin, M., Steinberg, D. K., and Trull, T.: An assessment of the use of sediment traps for estimating upper ocean particle fluxes, J. Mar. Res., 65, 345–416, https://doi.org/10.1357/002224007781567621, 2007.

Burd, A. B., Hansell, D. A., Steinberg, D. K., Anderson, T. R., Arístegui, J., Baltar, F., Beaupré, S. R., Buesseler, K. O., DeHairs, F., Jackson, G. A., Kadko, D. C., Koppelmann, R., Lampitt, R. S., Nagata, T., Reinthaler, T., Robinson, C., Robison, B. H., Tamburini, C., and Tanaka, T.: Assessing the apparent imbalance between geochemical and biochemical indicators of meso- and bathypelagic biological activity: What the @$♯! is wrong with present calculations

of carbon budgets?, Deep-Sea Res. Pt. II, 57, 1557–1571, https://doi.org/10.1016/j.dsr2.2010.02.022, 2010.

Dunne, J. P., Armstrong, R. A., Gnanadesikan, A., and Sarmiento, J. L.: Empirical and mechanistic models for the particle export ratio, Global Biogeochem. Cy., 19, GB4026, https://doi.org/10.1029/2004GB002390, 2005.

Ebersbach, F. and Trull, T. W.: Sinking particle properties from polyacrylamide gels during the DErguelen Ocean and Plateau compared Study (KEOPS): Zooplankton control of carbon export in an area of persistent natural iron inputs in the Southern Ocean, Limnol. Oceanogr., 53, 212–224, https://doi.org/10.4319/lo.2008.53.1.0212, 2008.

Ebersbach, F., Trull, T. W., Davies, D. M., and Bray, S. G.: Controls on mesopelagic particle fluxes in the Sub-Antarctic and Polar Frontal Zones in the Southern Ocean south of Australia in summer-Perspectives from free-drifting sediment traps, Deep-Res. Pt. II, 58, 2260–2276, https://doi.org/10.1016/j.dsr2.2011.05.025, 2011.

Estapa, M., Durkin, C., Buesseler, K., Johnson, R., and Feen, M.: Carbon flux from bio-optical profiling floats: Calibrating transmissometers for use as optical sediment traps, Deep-Res. Pt. I, 120, 100–111, https://doi.org/10.1016/j.dsr.2016.12.003, 2017.

Estapa, M. L., Buesseler, K., Boss, E., and Gerbi, G.: Autonomous, high-resolution observations of particle flux in the oligotrophic ocean, Biogeosciences, 10, 5517–5531, https://doi.org/10.5194/bg-10-5517-2013, 2013.

Falkowski, P. G., Barber, R. T., and Smetacek, V.: Biogeochemical Controls and Feedbacks on Ocean Primary Production, Science, 281, 200–206, https://doi.org/10.1126/science.281.5374.200, 1998.

Gardner, W. D., Richardson, M. J., and Smith Jr., W. O.: Seasonal patterns of water column particulate organic carbon and fluxes in the Ross Sea, Antarctica, Deep-Res. Pt. II, 47, 3423–3449, 2000.

Holser, R. R., Goni, M. A., and Hales, B.: Design and application of a semi-automated filtration system to study the distribution of particulate organic carbon in the water column of a coastal upwelling system, Mar. Chem., 123, 67–77, https://doi.org/10.1016/j.marchem.2010.10.001, 2011.

IUPAC: Compendium of Chemical Terminology, 2nd edn., compiled by: McNaught, A. D. and Wilkinson, A., Blackwell Scientific Publications, ISBN 0-9678550-9-8, last update: 24 February 2014; version: 2.3.3, Oxford, https://doi.org/10.1351/goldbook.A00513, 1997.

Lam, P. J. and Bishop, J. K. B.: High biomass, low export regimes in the Southern Ocean, Deep-Sea Res. Pt. II, 54, 601–638, https://doi.org/10.1016/j.dsr2.2007.01.013, 2007.

Lamborg, C. H., Buesseler, K. O., Valdes, J., Bertrand, C. H., Manganini, S., Pike, S., Bidigare, R., Steinberg, D., Wilson, S., and Trull, T.: The flux of bio- and lithogenic material associated with sinking particles in the mesopelagic "twilight zone" of the northwest and North Central Pacific Ocean, Deep-Sea Res. Pt. II, 55, 1540–1563, https://doi.org/10.1016/j.dsr2.2008.04.011, 2008

Mcdonnell, A. M. P., Boyd, P. W., and Buesseler, K. O.: Effects of sinking velocities and microbial respiration rates on the attenuation of particulate carbon fluxes, Global Biogeochem. Cy., 29, 175–193, https://doi.org/10.1002/2014GB004935, 2015.

Passow, U. and Carlson, C. A.: The biological pump in a high CO_2 world, Mar. Ecol. Prog. Ser., 470, 249–271, 2012.

Riley, J. S., Sanders, R., Marsay, C., Le Moigne, F. A. C., Achterberg, E. P., and Poulton, A. J.: The relative contribution of fast and slow sinking particles to ocean carbon export, Global Biogeochem. Cy., 26, GB1026, https://doi.org/10.1029/2011GB004085, 2012.

Saba, G. K. and Steinberg, D. K.: Abundance, composition, and sinking rates of fish fecal pellets in the Santa Barbara Channel, Sci. Rep., 2, 1–6, https://doi.org/10.1038/srep00716, 2012.

Siegel, D. A., Buesseler, K. O., Doney, S. C., Sailley, S. F., Behrenfeld, M. J., and Boyd, P. W.: Global assessment of ocean carbon export by combining satellite observations and food-web models, Global Biogeochem. Cy., 28, 181–196, https://doi.org/10.1002/2013GB004743, 2014.

Stanley, R. H. R., Doney, S. C., Jenkins, W. J., and Lott, D. E.: Apparent oxygen utilization rates calculated from tritium and helium-3 profiles at the Bermuda Atlantic Time-series Study site, Biogeosciences, 9, 1969–1983, https://doi.org/10.5194/bg-9-1969-2012, 2012.

Stukel, M. R., Ohman, M. D., Benitez-Nelson, C. R., and Landry, M. R.: Contributions of mesozooplankton to vertical carbon export in a coastal upwelling system, Mar. Ecol. Prog. Ser., 491, 47–65, https://doi.org/10.3354/meps10453, 2013.

Thunell, R. C.: Particle fluxes in a coastal upwelling zone: sediment trap results from Santa Barbara Basin, California, Deep-Sea Res. Pt. II, 45, 1863–1884, https://doi.org/10.1016/S0967-0645(98)80020-9, 1998.

Yao, X. and Schlitzer, R.: Assimilating water column and satellite data for marine export production estimation, Geosci. Model Dev., 6, 1575–1590, https://doi.org/10.5194/gmd-6-1575-2013, 2013.

Zaneveld, J. R. V.: Variation of optical sea parameters with depth, in: Lecture Series on Optics of the sea, 61, 1–22, 1973.